

Electronic Supplementary Information

Defect evolution of hierarchical SnO₂ aggregates for boosting CO₂ electrocatalytic reduction

Xueying Cao, Bari Wulan, Baohua Zhang, Dongxing Tan, Jintao Zhang*

Key Laboratory for Colloid and Interface Chemistry, Ministry of Education, School of Chemistry and Chemical Engineering, Shandong University, Jinan 250100, PR China.

*Corresponding author: E-mail: jtzhang@sdu.edu.cn (Jintao Zhang)

Experiments

1. In situ ATR-SEIRAS test:

Au film deposition: Due to the low intensity of ECRR intermediates, Au film was used to increase the Infrared signals. Before deposition, the Si crystal was immersed in Piranha solution (a solution with a volume ratio of H_2SO_4 to H_2O_2 of 3:1) for 20 min to clean the organic contaminants on crystal. In order to improve adhesion of the Au film, the reflecting plane of the Si crystal was then immersed in 40 % NH_4F solution for 5 min to remove the oxide layer and generate a hydrogen-terminated surface. After that, the reflecting plane of Si crystal was immersed in a mixture of 85 μL of 40 % HF and 5 mL of Au plating solution for 5 min at 55 °C to obtain the final Au film.

ATR-SEIRAS sample prepared: The electrocatalyst ink was prepared by adding 3 mg sample into 200 μL ethanol-water solution containing 20 μL 0.5 vol% Nafion solution. The electrodes were made by dropping 50 μL ink on Si prism over Au film and dried with N_2 flow.

ATR-SEIRAS experiments: The Si prism with incidence of 55° angle, a Pt foil and an Ag/AgCl electrode were served as working electrode, counter electrode and reference electrode, respectively. An H-type cell separated by Nafion membrane was used to accommodate the Si prism. A Thermo Fisher Nicolet IS50 spectrometer equipped with MCT detector and a Pike Technologies VeeMAX III ATR accessory was employed for the electrochemical ATR-SEIRAS. Firstly, a 5 L/min N_2 flow was aerated continuously to purge the optical path system to reduce the influence of CO_2 (g) and H_2O (g) in air. All spectra were collected with a 4 cm^{-1} resolution and 32 scans. The electrolyte was CO_2 -saturated 0.5 M KHCO_3 aqueous solution.

2. Differential Electrochemical Mass Spectrometry (DEMS):

Preparation of working electrode: The working electrode for the DEMS measurements was a commercially available glassy carbon electrode. The working electrode was polished using progressively smaller sizes of Al_2O_3 (1, 0.05 and 0.03 μm), and sonicated in ethanol, water and dried under nitrogen. Then, the working electrodes were prepared by dropping 10 μl ink on disk area.

DEMS experiments: The DEMS measurements were carried out using a thin layer flow cell under the continuous mass transport conditions. The volatile or the dissolved gaseous products were evaporated in the high vacuum of a prechamber, and the remaining species were directed to a main chamber, where the sample was analyzed by a commercial quadrupole mass spectrometer (Prisma Plus). The glassy carbon, a Pt wire and a saturated Ag/AgCl electrode were served as working electrode, counter electrode and reference electrode, respectively. In this thin layer flow cell configuration, the working electrode was pressed against a 0.3 mm spacer that separated it from the flow cell. The reference electrode was positioned in the electrolyte inlet and the counter electrode was positioned in the electrolyte outlet. The electrode was separated from the porous PTFE membrane. The gap between the working electrode and the flow cell formed the thin-layer cell for DEMS determination. The CO_2 -saturated 0.5 M KHCO_3 electrolyte solution was flowed at a rate of 10 $\mu\text{L/s}$. The volatile products of the electrochemical reactions were monitored at different values of m/z ionic signals.

3. Computational Details:

Periodic density functional theory (DFT) calculations were performed with the Perdew-Burke-Ernzerhof (PBE) exchange-correlation functional¹ and the projector-augmented wave (PAW)

method.^{2, 3} The Vienna ab initio Simulation Program (VASP) package was used for the calculations in this work.^{4, 5} The recommended default potentials were employed for the C, H, O element. For the Sn atom, the Sn (5s, 5p) was treated as valence state. An energy cutoff of 400 eV was used throughout this work, with spin polarization also considered. Gaussian smearing with a width of 0.05 eV was applied for the structural optimizations. The electronic energy of the supercell was converged to 10⁻⁶ eV in the self-consistent field calculations, whereas the force on each relaxed atom was converged to 0.02 eV/Å in the ionic relaxation calculations.

For the oxygen deficit SnO₂ slab, we constructed the SnO₂ (110) surface as the substrate. And three types of structure models including clean SnO₂ (110), Sn/SnO₂ (110) and Sn/ SnO_{2-x} (110) were built with different Sn/O ratios. For the SnO₂ (110) substrate, a p-(3×2) supercell was constructed with vacuum layer of 15 Å inserted between adjacent slabs, and half of the bottom layers were kept constraint during optimizations. A Γ -centred Monkhorst-Pack k-point mesh of (1×1×1) was applied throughout the calculations.

The Gibbs free energy for each species in a given elementary step was calculated as $G = E_{elec} + EZPE - T*S$, where E_{elec} is the electronic energy at 0 K from the DFT calculation, EZPE is the zero-point energy term, and the pV is the constant-pressure heat capacity. For gaseous molecules including HCOOH, H₂, and CO₂, the entropies were obtained from NIST chemistry webbook.⁶ For surface-adsorbed species, all 3N degrees of freedom of the adsorbate were treated as harmonic vibrations, and the entropy was calculated as a sum of the contributions from these vibrational motions.

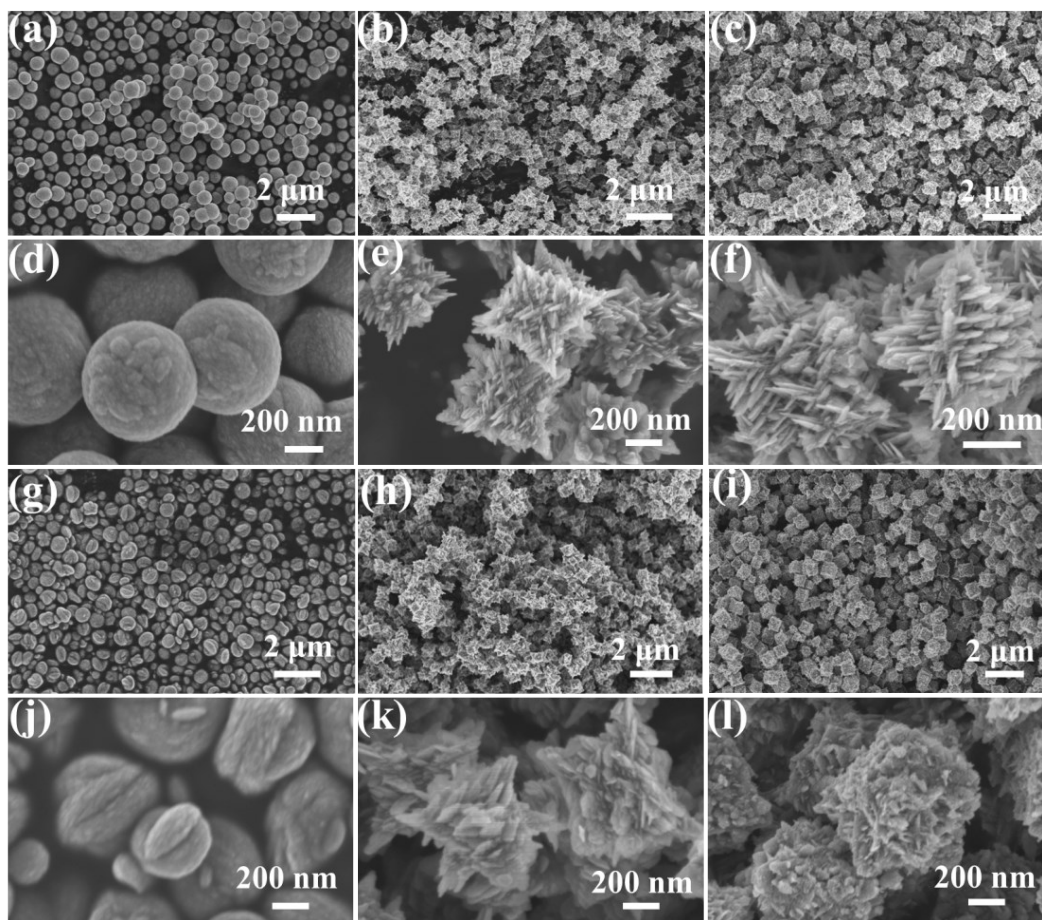


Fig. S1. SEM images of (a, d) SnO₂(p)-10, (b, e) SnO₂(p)-20, (c, f) SnO₂(p)-30, (g, j) SnO₂-10, (h, k) SnO₂-20 and (i, l) SnO₂-30.

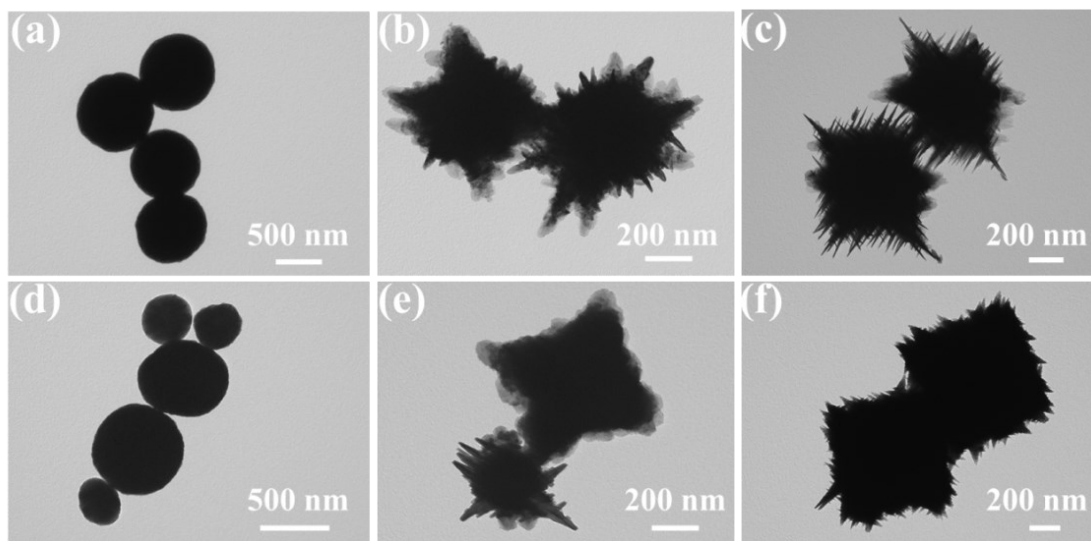


Fig. S2. TEM images of (a) SnO₂(p)-10, (b) SnO₂(p)-20, (c) SnO₂(p)-30, (d) SnO₂-10, (e) SnO₂-20 and (f) SnO₂-30.

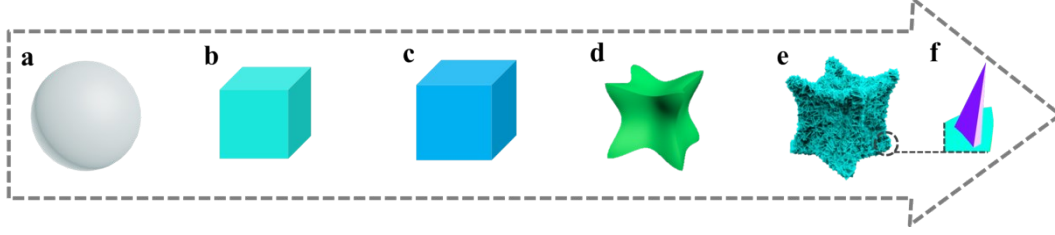


Fig. S3. Effect of the morphology on catalyst specific surface area.

When the densities of all above aggregates are assumed to be one, V , S are the volume and the superficial area, respectively. The specific surface area, S_s , can be obtained, $S_s = S/V$.

For the sphere, a with a radius (r) of 300 nm, $V_a = \frac{4}{3}\pi r^3$, $S_a = 4\pi r^2$, $S_{sa} = \frac{3}{r} = 0.01$;

For the cube, b with a side length (l) of 400 nm, $V_b = l^3$, $S_b = 6l^2$, $S_{sb} = \frac{6}{l} = 0.015$;

For the cube, c with a side length (l) of 500 nm, $V_c = l^3$, $S_c = 6l^2$, $S_{sc} = \frac{6}{l} = 0.012$;

For the concave cube, d with a side length (l) of 400 nm, the depth of the concave is 85 nm (Fig. 1c), a four pyramid with side length (l_p) of 400 nm and height (h) of 85 nm represents the volume and surface area of the recessed part. Thus,

$$V_d = l^3 - 6 \times \frac{1}{3} l_p^2 \times h, S_d = 6 \times 4 \times \frac{l_p \times \sqrt{(\frac{l_p}{2})^2 + (h)^2}}{2}, S_{sd} = 0.028;$$

For the concave cube, e is assembled by many nanosheets (f), a small pyramid with side length (l_p) of 30 nm, thickness (t) of 10 nm and height (h) of 60 nm represents the nanosheet.

$$V_f = \frac{1}{3} l_p \times t \times h, S_f = 2 \times \left(\frac{l_p \times \sqrt{(\frac{l_p}{2})^2 + (h)^2}}{2} + \frac{t \times \sqrt{(\frac{l_p}{2})^2 + (h)^2}}{2} \right),$$

$$S_{sf} = 0.353, 0.028 < S_{se} < 0.353.$$

Thus, the specific surface areas of these aggregations satisfy the following order:

$$S_{sa} < S_{sc} < S_{sb} < S_{sd} < S_{se}$$

It can be seen that the concave cube assembled with small nanosheets is able to provide larger surface area.

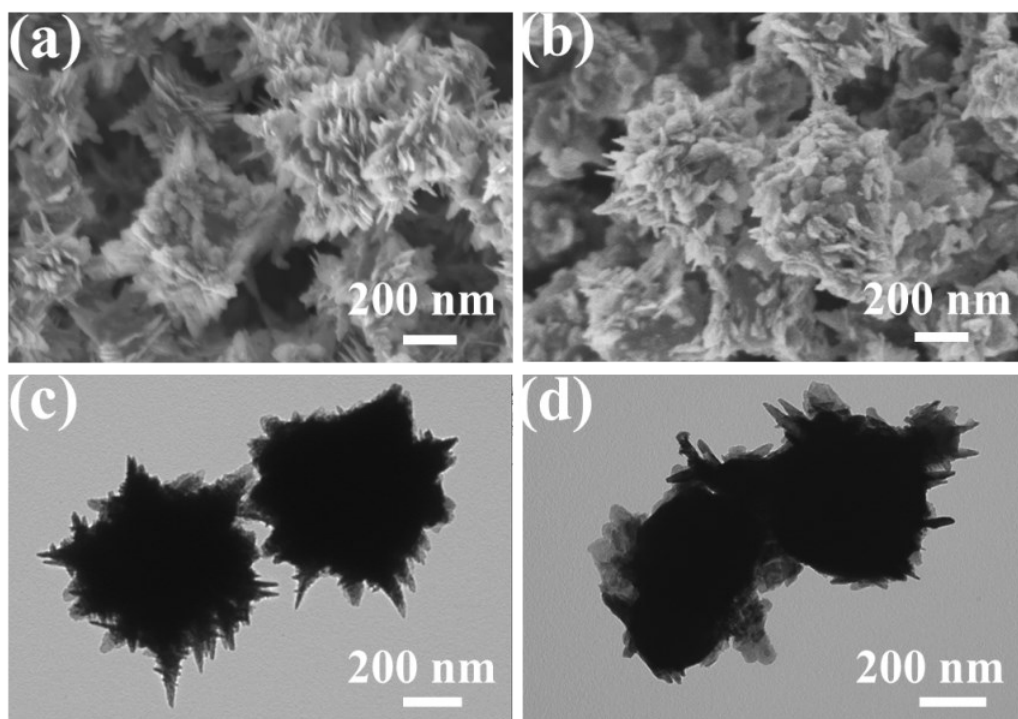


Fig. S4. SEM and TEM images of (a,c) Sn/SnO₂-1h and (b,d) Sn/SnO₂-3h.

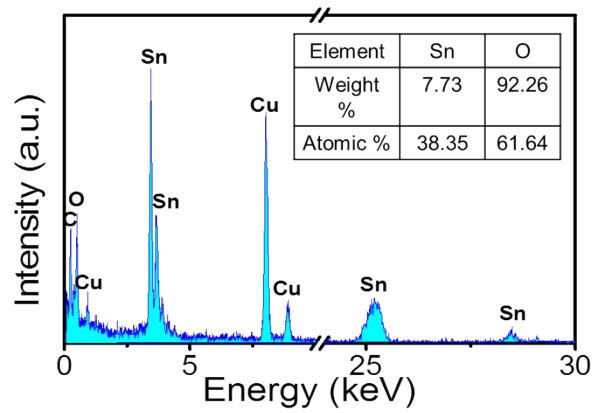


Fig. S5. TEM EDS spectrum of Sn/SnO₂-2h.

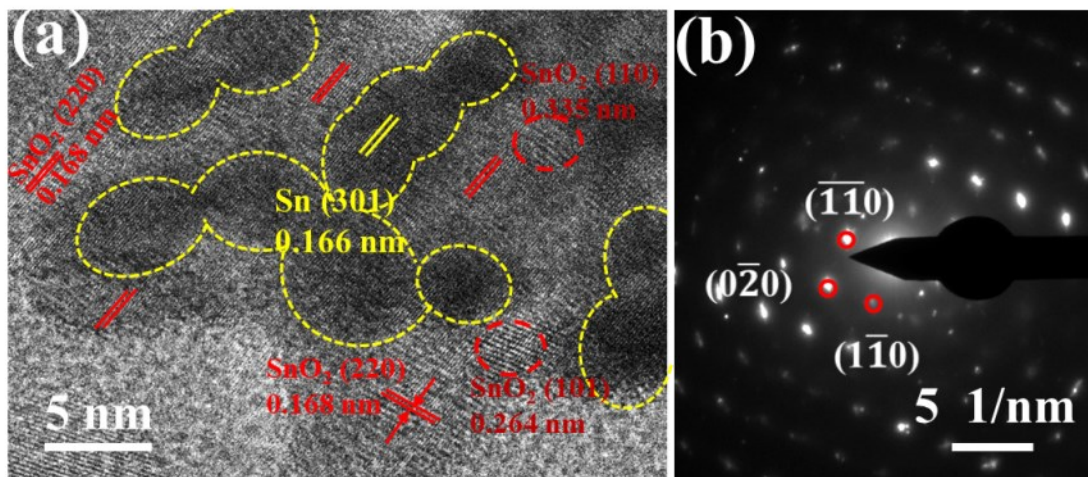


Fig. S6. (a) HRTEM image and (b) SAED pattern of Sn/SnO₂-2h.

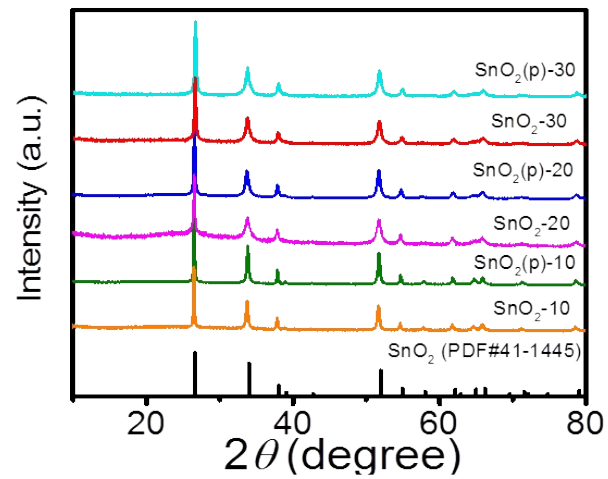


Fig. S7. XRD patterns and of SnO₂(p)-10, SnO₂(p)-20, SnO₂(p)-30, SnO₂-10, SnO₂-20 and SnO₂-30.

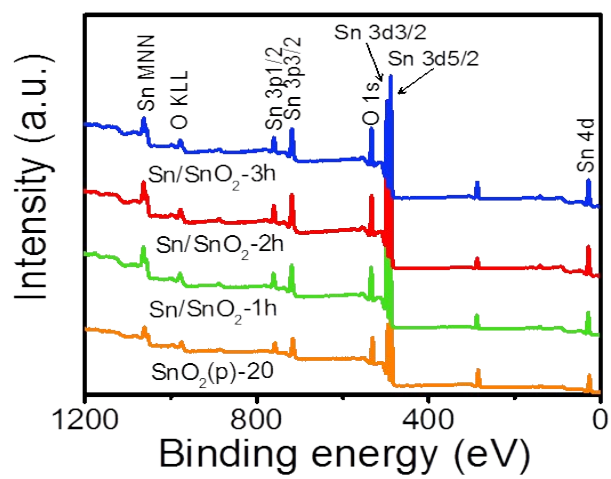


Fig. S8. XPS survey spectra of SnO₂(p)-20, Sn/SnO₂-1h, Sn/SnO₂-2h and Sn/SnO₂-3h.

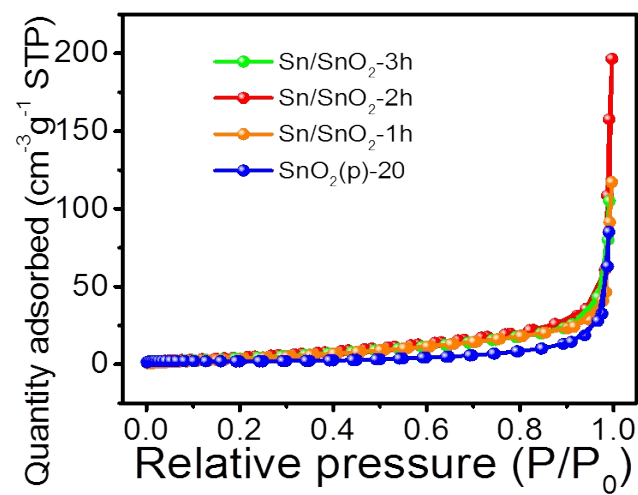


Fig. S9. Nitrogen adsorption-desorption isotherms of SnO₂(p)-20, Sn/SnO₂-1h, Sn/SnO₂-2h and Sn/SnO₂-3h.

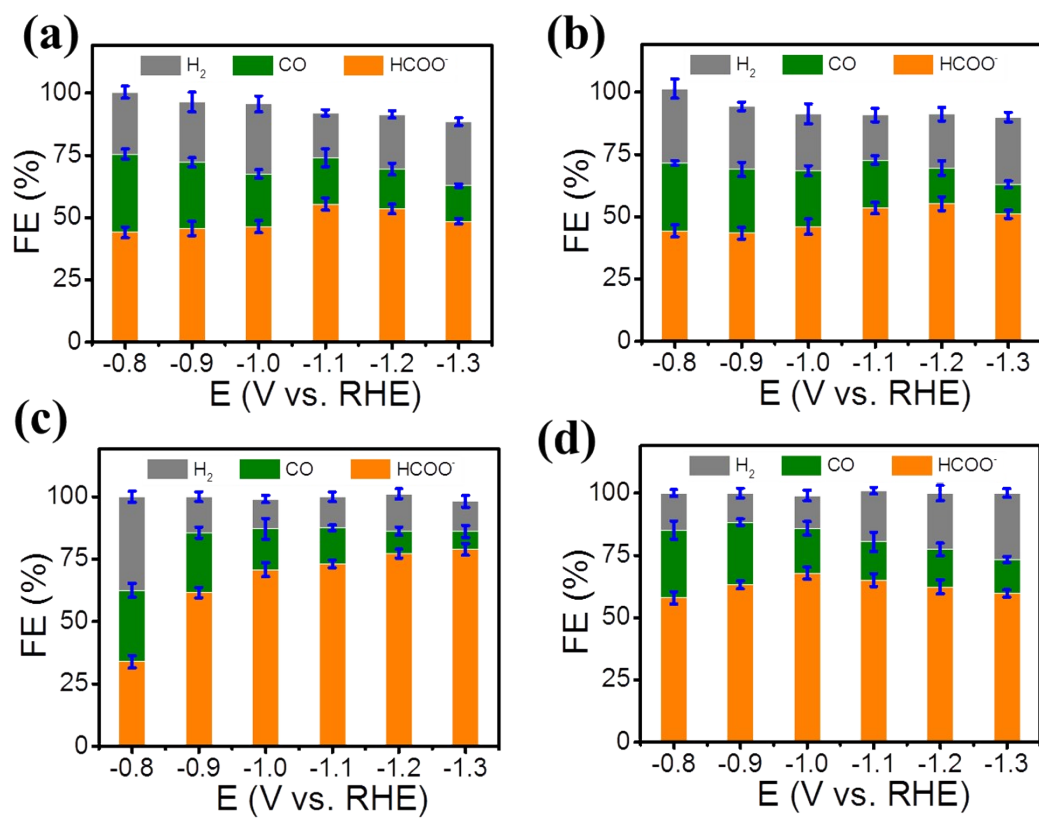


Fig. S10. FEs for CO, HCOO⁻, and H₂ at different voltages for (a) SnO₂(p)-10, (b) SnO₂(p)-30, (c) Sn/SnO₂-1h and (d) Sn/SnO₂-3h.

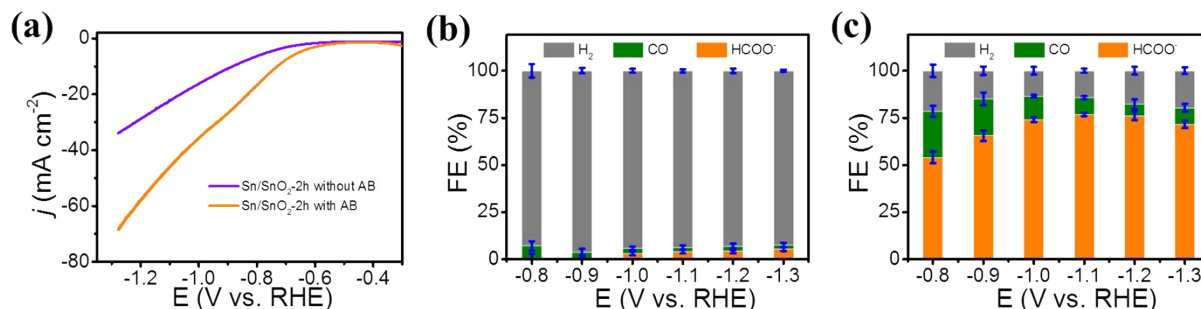


Fig. S11. (a) LSV curves for Sn/SnO₂-2h electrode with and without acetylene black (AB). FEs for CO, HCOO⁻, and H₂ at different voltages for (b) pure AB electrode and (c) Sn/SnO₂-2h electrode without AB.

The presence of acetylene black (AB) would improve the electrical conductivity and the dispersion of electrocatalysts (Fig. S11a) to enhance the ECRR. Especially, the pure AB electrode exhibits high FE for hydrogen evolution (Fig. S11b). The result suggests the hydrogen evolution is the key reaction at the AB electrode in the applied potential range. Meanwhile, the control experiment based on the Sn/SnO₂-2h electrode without AB was also carried out and shown in Fig. S11c. Compared with the FEs at the Sn/SnO₂-2h electrode with AB (Fig. 3d), the slight changes on the Faraday efficiency at Sn/SnO₂-2h electrode without AB are observed. The results suggest the presence of AB improves the current density for carbon dioxide reaction by improving the electrical conductivity and dispersion of electrocatalysts.

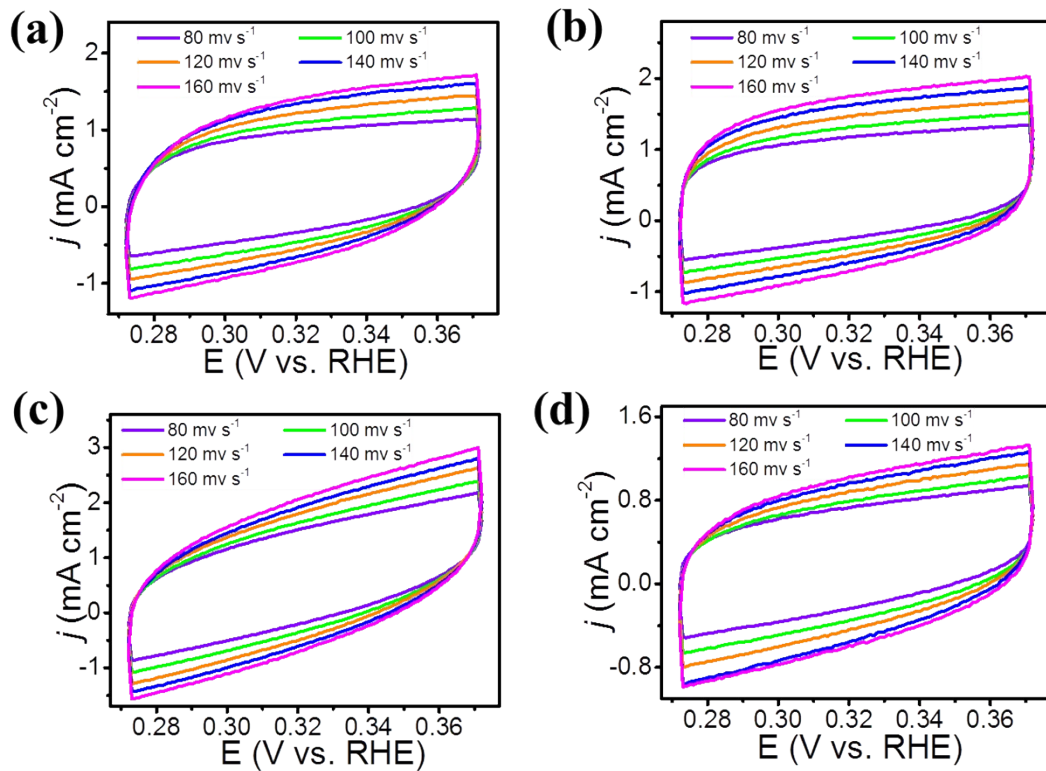


Fig. S12. (a-d) CV curves for SnO₂(p)-20, Sn/SnO₂-1h, Sn/SnO₂-2h and Sn/SnO₂-3h, respectively, at different scan rates.

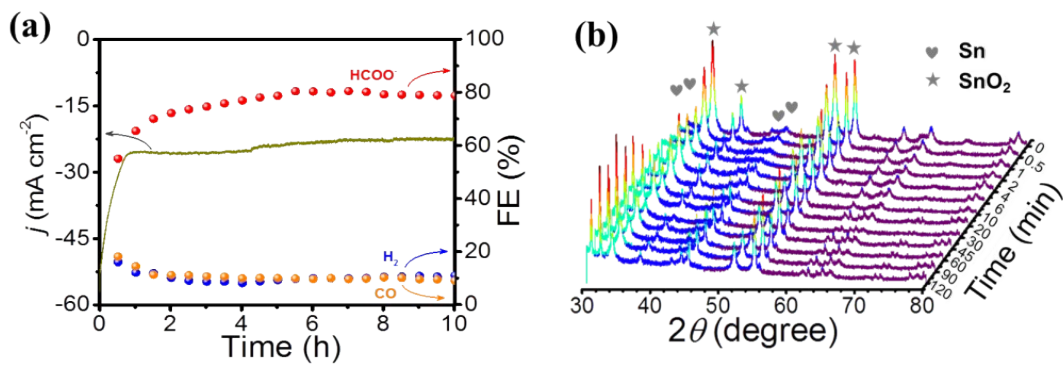


Fig. S13. (a) Long-term stability tests and FEs for SnO₂(p)-20. (b) Quasi in situ XRD measurements during CO₂ electroreduction at -1.1 V vs. RHE for SnO₂(p)-20.

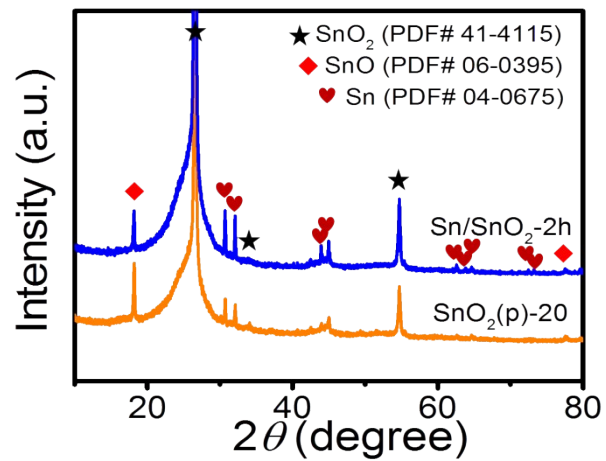


Fig. S14. XRD patterns of SnO₂(p)-20 and Sn/SnO₂-2h samples after long-term stability tests.

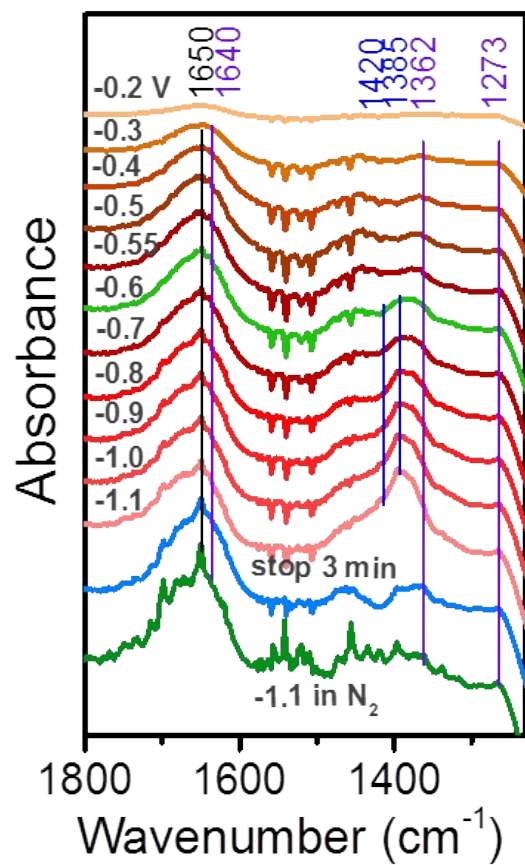


Fig. S15. *In situ* ATR-SEIRAS spectra collected during different potential scans on Au film electrodes of SnO₂(p)-20.

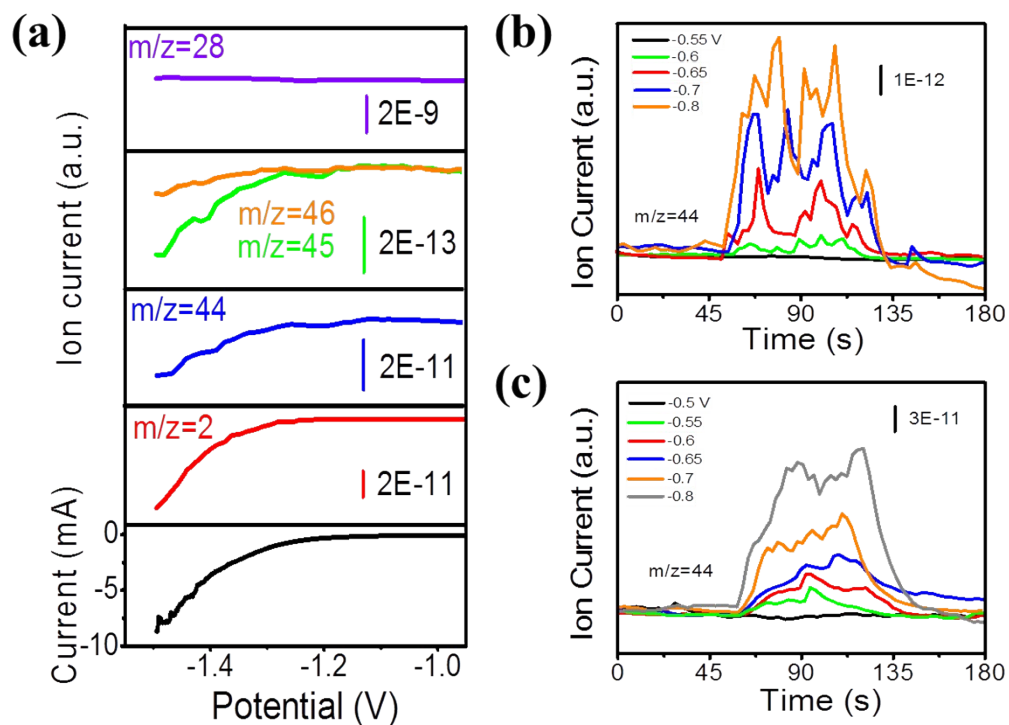


Fig. S16. (a) DEMS in the presence of CO₂ on SnO₂(p)-20 electrode. Bottom: LSV curves at scan rate of 5 mV/s in CO₂ saturated 0.5M KHCO₃ solution. Upper: Ion current signals during LSV scans. H₂ (m/z=2), HCOOH (m/z=28, 44, 45, 46), CO (m/z=28). Ion currents for HCOOH by DEMS with dependence of different potentials of (b) SnO₂(p)-20 and (c) Sn/SnO₂-2h samples.

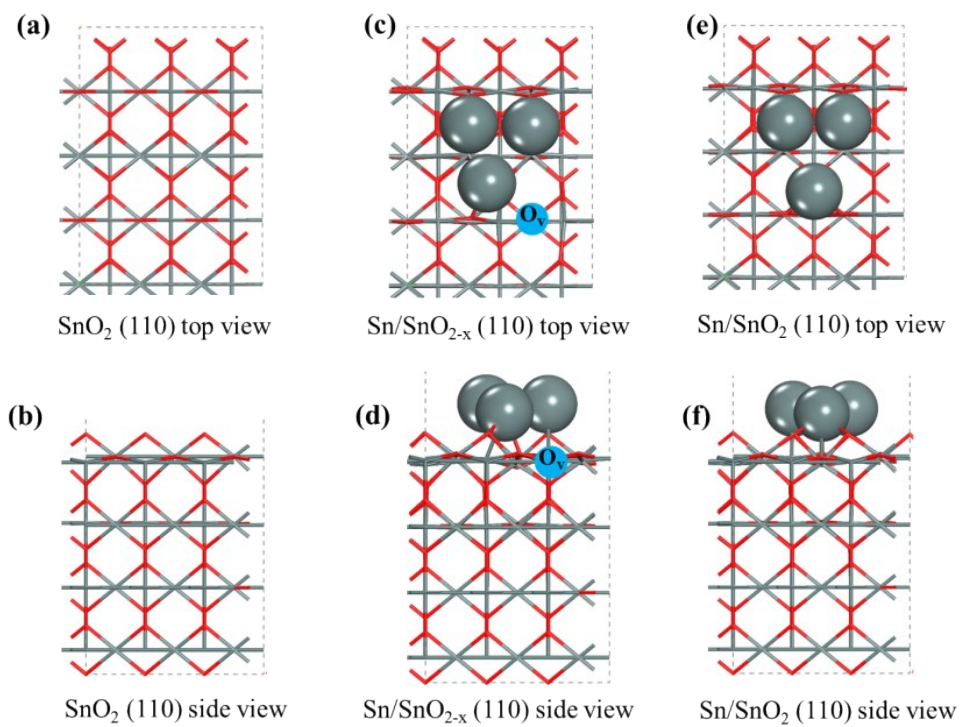


Fig. S17. Top and side views of optimized structure of (a,b) SnO₂ (110), (c,d) Sn/SnO_{2-x} (110), and (e,f) Sn/SnO₂ (110).

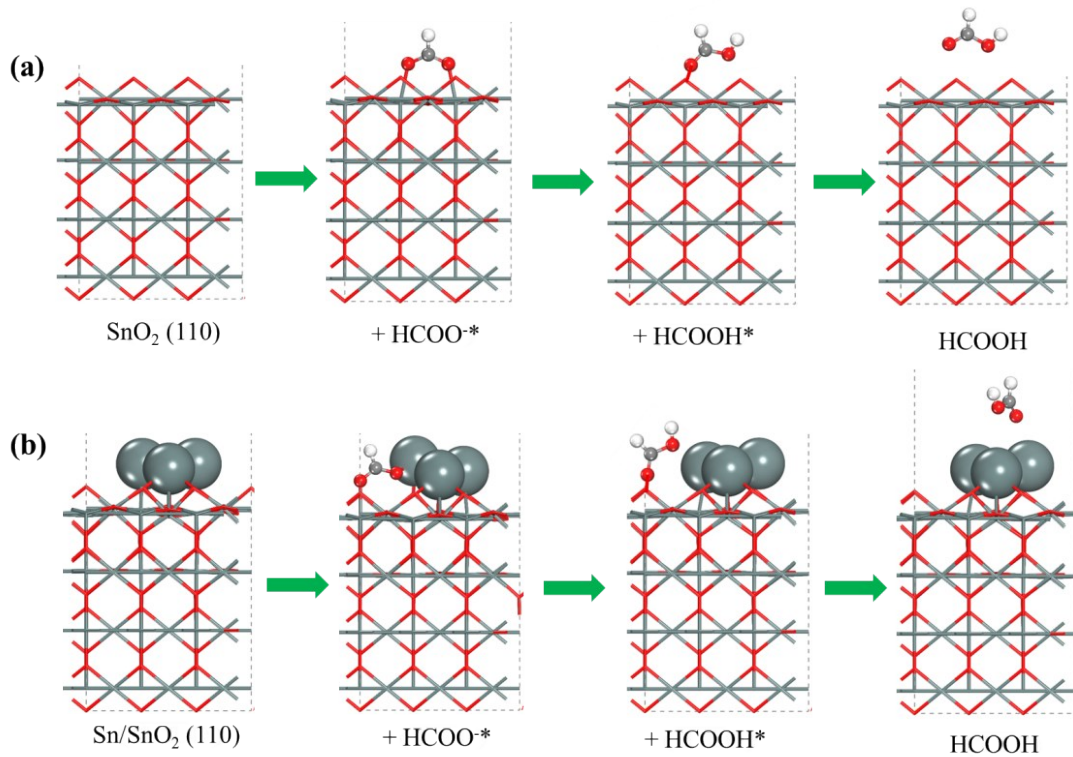


Fig. S18. Reaction pathways of ECRR to formate on (a) SnO₂ (110) plane, and (b) Sn/SnO₂ (110) plane (gray, red, brown and white spheres represent Sn, O, C and H atoms, respectively).

Table S1. The performance comparison of various electrocatalysts for carbon dioxide reduction.

Catalyst	FE _{HCOO} - (%)	FE _{Cl} (%)	E (V vs. RHE)	Electrolyte	Ref.
Sn/SnO ₂ -1h	77.2	92.2	-1.2	0.5 M KHCO ₃	This work
Sn/SnO ₂ -2h	78.8	92.5	-1.0	0.5 M KHCO ₃	
Sn/SnO ₂ -3h	63.2	88.3	-0.9	0.5 M KHCO ₃	
SnO ₂ /graphene	93.6	—	-1.8	0.1 M NaHCO ₃	7
SnO ₂ /carbon black	86	—	-1.16	0.1 M NaHCO ₃	7
Sn quantum sheets/GO	89	—	-1.8 (vs. SCE)	0.1 M NaHCO ₃	8
AgSn/SnO _x	80	—	-0.8	0.5 M NaHCO ₃	9
SnO ₂ porous nanowires	80	—	-0.8	0.1 M NaHCO ₃	10
Sn NPs	58	~90	-0.8	0.1 M KHCO ₃	10
Ultra-small SnO ₂ NPS	64	—	-1.12	1.0 M KHCO ₃	11
Ultra-small SnO	66	—	-0.9	0.5 M KHCO ₃	12
Urchin-like SnO ₂	62	—	-1.0	0.5 M KHCO ₃	13
SnO ₂ quantum wires	80	90	-1.16	0.1 M KHCO ₃	14
1D SnO ₂ with wire-in-tube	63	93	-0.99	0.1 M KHCO ₃	15
Zn ₂ SnO ₄ /SnO ₂	77	—	-1.08	0.1 M KHCO ₃	16
Sn modified N-doped CF	62	91	-0.8	0.5 M KHCO ₃	17
SnO ₂ /Sn	70	—	-1.05	0.1 M KHCO ₃	18
Sn/SnO _x /Ti foil	~40	~97	-0.7	0.5 M NaHCO ₃	19
Electrodeposited Sn GDE	71	82	-1.1	0.5 M NaHCO ₃	20
SnO ₂ GDE	68	—	-1.28	0.5 M KHCO ₃	21
Sn GDE	~73	—	-1.1	0.5 M KHCO ₃	22
Sn foil	63.5	—	-1.37	0.5 M KHCO ₃	23
SnO _x dendrite/Sn foil	71.6	83.4	-1.36	0.1 M NaHCO ₃	24
Single atom Sn ^{δ+} on N-G	74.3	—	-1.6(vs. SCE)	0.25 M KHCO ₃	25

References

1. J. P. Perdew, K. Burke, M. Ernzerhof, *Phys. Rev. Lett.*, 1996, **77**, 3865-3868.
2. G. Kresse, D. Joubert, *Phys. Rev. B*, 1999, **59**, 1758-1775.
3. P. E. Blöchl, *Phys. Rev. B*, 1994, **50**, 17953-17979.
4. G. Kresse, J. Furthmüller, *Phys. Rev. B*, 1996, **54**, 11169-11186.
5. G. Kresse, J. Furthmüller, *Comp. Mater. Sci*, 1996, **6**, 15-50.
6. P. Linstorm, *J. Phys. Chem. Ref. Data, Monograph*, 1998, **9**, 1-1951.
7. S. Zhang, P. Kang, T. J. Meyer, *J. Am. Chem. Soc.*, 2014, **136**, 1734-1737.
8. F. Lei, W. Liu, Y. Sun, J. Xu, K. Liu, L. Liang, T. Yao, B. Pan, S. Wei, Y. Xie, *Nat. Commun.*, 2016, **7**, 12697.
9. W. Luc, C. Collins, S. Wang, H. Xin, K. He, Y. Kang, F. Jiao, *J. Am. Chem. Soc.*, 2017, **139**, 1885-1893.
10. B. Kumar, V. Atla, J. P. Brian, S. Kumari, T. Q. Nguyen, M. Sunkara, J. M. Spurgeon, *Angew. Chem., Int. Ed.*, 2017, **56**, 3645-3649.
11. C. Liang, B. Kim, S. Yang, L. Yang, C. Francisco Woellner, Z. Li, R. Vajtai, W. Yang, J. Wu, P. J. A. Kenis, Pulickel M. Ajayan, *Angew. Chem., Int. Ed.*, 2018, **6**, 10313-10319.
12. J. Gu, F. Heroguel, J. Luterbacher, X. Hu, *Angew. Chem., Int. Ed.*, 2018, **57**, 2943-2947.
13. Y. Liu, M. Fan, X. Zhang, Q. Zhang, D. Guay, J. Qiao, *Electrochim. Acta*, 2017, **248**, 123-132.
14. S. Liu, J. Xiao, X. F. Lu, J. Wang, X. Wang, X. W. Lou, *Angew. Chem., Int. Ed.*, 2019, **58**, 8499-8503.
15. L. Fan, Z. Xia, M. Xu, Y. Lu, Z. Li, *Adv. Funct. Mater.*, 2018, **28**, 1706289.
16. K. Wang, D. Liu, P. Deng, L. Liu, S. Lu, Z. Sun, Y. Ma, Y. Wang, M. Li, B. Y. Xia, C. Xiao, S. Ding, *Nano Energy*, 2019, **64**, 103954.
17. Y. Zhao, J. Liang, C. Wang, J. Ma, G. G. Wallace, *Adv. Energy Mater.*, 2018, **8**, 1702524.
18. J. E. Pander, M. F. Baruch, A. B. Bocarsly, *ACS Catal.*, 2016, **6**, 7824-7833.
19. Y. Chen, M. W. Kanan, *J. Am. Chem. Soc.*, 2012, **134**, 1986-1989.
20. E. Irtem, T. Andreu, A. Parra, M. D. Hernández-Alonso, S. García Rodríguez, J. M. Riesco García, G. Penelas Pérez, J. R. Morante, *J. Mater. Chem. A*, 2016, **4**, 13582-13588.
21. Y. Fu, Y. Liu, Y. Li, J. Qiao, X. D. Zhou, *ECS Trans.*, 2015, **66**, 53-59.
22. Q. Wang, H. Dong, H. Yu, *RSC Adv.*, 2014, **4**, 59970-59976.
23. J. Wu, F. Risalvato, X. D. Zhou, *ECS Trans.*, 2019, **41**, 49-60.
24. D. H. Won, C. H. Choi, J. Chung, M. W. Chung, E. H. Kim, S. I. Woo, *ChemSusChem*, 2015, **8**, 3092-3098.
25. X. Zu, X. Li, W. Liu, Y. Sun, J. Xu, T. Yao, W. Yan, S. Gao, C. Wang, S. Wei, Y. Xie, *Adv. Mater.*, 2019, **31**, 1808135.